

# Magnetic Field Observations on Interhemispheric Conjugate Chains

D. R. Weimer<sup>1,2</sup>, C. R. Clauer<sup>1,2</sup>, Z. Xu<sup>1,2</sup>, S. Coyle<sup>1</sup>, and M. D. Hartinger<sup>3</sup>

<sup>1</sup>Center for Space Science and Engineering Research, Virginia Tech, Blacksburg, Virginia, USA

<sup>2</sup>National Institute of Aerospace, Hampton, Virginia, USA

<sup>3</sup>Space Science Institute, Boulder, CO, USA

## Key Points:

- Magnetic field measurements are obtained from magnetic conjugate points in both hemispheres
- Under optimal conditions the conjugate magnetic fields are very similar, provided that signs are reversed on two of the vector components
- More often the fields differ due to different seasonal conductivities and asymmetrical driving by the magnetic field in the solar wind

**Abstract**

A chain of magnetometers has been placed in Antarctica for comparisons with magnetic field measurements taken in the northern hemisphere. The locations were chosen to be on magnetic field lines that connect to magnetometers on the western coast of Greenland, despite the difficulty of reaching and working at such remote locations. We report on some basic comparisons of the similarities and differences in the conjugate measurements. Our results presented here confirm that the conjugate sites do have very similar (symmetric) magnetic perturbations in a handful of cases, as expected. Sign reversals are required for two components in order to obtain this agreement, which is not commonly known. More frequently, a strong Y component of the Interplanetary Magnetic Field (IMF) breaks the symmetry, as well as the unequal conductivities in the opposite hemispheres, as shown in two examples. In one event the IMF Y component reversed signs twice within two hours, while the magnetometer chains were approaching local noon. This switch provided an opportunity to observe the effects at the conjugate locations and to measure time lags. It was found that the magnetic fields at the most poleward sites started to respond to the sudden IMF reversals 18 min after the IMF reaches the bow shock, a measure of the time it takes for the electromagnetic signal to travel to the magnetopause, and then along magnetic field lines to the polar ionospheres. An additional 9 to 14 min is required for the magnetic perturbations to complete their transition.

**Plain Language Summary**

Space science research has long relied on magnetometer measurements in the northern hemisphere to detect and observe the flow of currents in the ionosphere and magnetosphere. In the past few years it has become possible to acquire magnetic field measurements in the southern polar region as well, as a result of the placement of a chain of magnetometer stations in a remote part of Antarctica. Each of these magnetometers were placed where the Earth's magnetic field connects to an existing magnetometer in the northern hemisphere, on the western coast of Greenland. The locations follow a roughly north-south meridian in geomagnetic coordinates. These "conjugate" magnetometer chains are useful for observing the similarities and differences between the ionospheric currents flowing in opposite hemispheres as a result of the solar wind's interaction with the Earth's magnetosphere. This paper presents results showing how the inter-hemispheric measurements are very similar in some cases, but only if the signs of two of the vector compo-

46 nents are reversed. In other cases the magnetic fields in the northern and southern hemi-  
47 sphere are different, mainly due to the summer-winter differences in conductivity. The  
48 conjugate measurement will be useful for future space science research.

## 49 **1 Introduction**

50 Due to the dipole nature of Earth's magnetic field, electric fields and plasma mo-  
51 tions in the outer magnetosphere map to the ionosphere at polar and auroral latitudes  
52 in both hemispheres. The resulting currents that flow in the ionosphere can be detected  
53 by their magnetic signature on the ground. Ground arrays of magnetometers at high lat-  
54 itudes are particularly useful for monitoring such space weather phenomena, and learn-  
55 ing about the interactions between the solar wind, the magnetosphere, and ionosphere.  
56 Arrays of instruments in the polar regions can be used to supplement sparse observa-  
57 tions from satellites in space. Measurements from polar instruments are also vital to the  
58 validation of global numerical models that may be used to describe and forecast space  
59 weather phenomena. It is, therefore, increasingly important to deploy arrays of geophys-  
60 ical instruments in polar regions to advance our understanding of the complex electro-  
61 dynamic interactions that comprise space weather. It is assumed that the magnetome-  
62 ters at conjugate locations (at opposite ends of the magnetic field lines) should show  
63 similar magnetic perturbations due to the magnetospheric flows, electric fields, and currents. On  
64 the other hand, differences should be expected because of the considerable asymmetries  
65 between the two hemispheres. For example, solar illumination differences between the  
66 summer and winter hemisphere produce large asymmetries in the conductance in the two  
67 polar ionospheres (Ostgaard & Laundal, 2012). The magnetic field in the Southern Hemi-  
68 sphere is significantly weaker, which also influences conductivity (Laundal et al., 2017).  
69 For these reasons the examination of simultaneous data from both the northern and south-  
70 ern polar regions is very important for understanding the causes and consequences of hemi-  
71 spheric asymmetries and, more broadly, to space science research. The results presented  
72 here use data from two ground magnetometer chains that are located at conjugate lo-  
73 cations in both hemispheres. The similarities and differences in these data are exam-  
74 ined. This investigation concerns magnetic perturbations varying on timescales on the  
75 order of 1–10 min.

## 2 Data

A magnetometer chain that is located on the west coast of Greenland is operated by the Technical University of Denmark (DTU). These stations were first established in 1981–1986. Most of the magnetometers in this chain are variometers, except for three that are geomagnetic observatories ([https://www.space.dtu.dk/English/Research/Scientific\\_data\\_and\\_models/Magnetic\\_Ground\\_Stations.aspx](https://www.space.dtu.dk/English/Research/Scientific_data_and_models/Magnetic_Ground_Stations.aspx)) that have accurate, absolute calibrations. Another chain is positioned on the East Antarctic plateau and is operated by Virginia Tech. The instrumentation is referred to as Autonomous Adaptive Low-Power Instrument Platforms (AAL-PIP) (Clauer et al., 2014), while the chain itself can be referred to as PENGUIn (Polar Experimental Network for Geospace Upper atmosphere Investigations). The six PENGUIn stations were flown to the remote Antarctic plateau in 2008–2016, at a pace of one to two per year, with some return visits for repairs. As illustrated in the photos by Clauer et al. (2014), the installation of these systems involved high altitude, cold-weather camping at each site. The AAL-PIP and Greenland data are both in sensor coordinates northward, eastward, and vertical (NEZ). The northward axis of the magnetometers are aligned with the local magnetic field and the Z axis is pointed downward, so that the orientation of the eastward axis (in local magnetic coordinates) results through the right-hand rule. The units of all components are nT.

By design the AAL-PIP stations were placed at the magnetic conjugate points of the existing Western Greenland stations, with are situated (approximately) along the 40° magnetic meridian. The intended coordinates for these stations was determined through use of the International Geomagnetic Reference Field (IGRF), while the final exact locations were determined by whatever landing sites the plane pilots deemed to be suitable. The three-letter site identification codes of the Greenland stations are derived from the location names in the local, native language and the codes for the Antarctic stations are simply numbered from 0 to 5 with a “PG” prefix. The geographic and magnetic coordinates of these stations are listed in Table 1. Magnetic apex coordinates are used (VanZandt et al., 1972; Richmond, 1995), derived from the IGRF 2015 model. The PENGUIn and Greenland magnetometer data have previously been used to investigate interhemispheric asymmetries in magnetic perturbations (Hartinger et al., 2016, 2017; Martines-Bedenko et al., 2018; Xu et al., 2017, 2020).

**Table 1.** Coordinates of the ground magnetometers used in this study

Northern Hemisphere Magnetometers					Southern Hemisphere Magnetometers				
Site ID	Geodetic		Geomagnetic <sup>a</sup>		Site ID	Geodetic		Geomagnetic <sup>a</sup>	
Code	°Lat.	°Lon.	°Lat.	°Lon.	Code	°Lat.	°Lon.	°Lat.	°Lon.
UPN	72.78	303.85	78.21	38.50	PG0	-83.67	88.68	-78.45	38.42
UMQ	70.68	307.87	75.62	41.07	PG1	-84.50	77.20	-77.06	37.51
GDH	69.25	306.47	74.46	38.08	PG2	-84.42	57.96	-75.34	39.22
ATU	67.93	306.43	73.18	37.03	PG3	-84.81	37.63	-73.61	36.82
SKT	65.42	307.10	70.58	36.26	PG4	-83.34	12.25	-70.88	36.46
GHB	64.17	308.27	69.12	36.95	PG5	-81.96	5.71	-69.49	37.31

<sup>a</sup>Geomagnetic locations are apex coordinates, calculated with the IGRF 2015 Model.

108 Interestingly, a comparison with the magnetic coordinates calculated with the IGRF  
 109 2020 model indicated that in five years the Antarctic sites had moved equatorward by  
 110 0.35 – 0.41°, while the Greenland sites moved poleward by 0.12 – 0.16°. Additionally,  
 111 Global Positioning System (GPS) instrumentation included on the platforms also showed  
 112 that the ice sheet on which the stations rest is slowly shifting. The speed varies from a  
 113 few meters per year for the PG0, PG1, PG2, and PG3 (those closest to the poles) to a  
 114 few tens of meters per year at PG4 and PG5, which are closest to the coast. Generally  
 115 speaking, the stations move towards the coast, the closer to the coast the faster the speed.  
 116 For PG3, PG4, and PG5 this is northeastward, toward Halley. PG2, PG1, and PG0 move  
 117 more towards McMurdo.

### 118 3 Symmetric Magnetic Fields Observed at Magnetic Conjugate Points

119 Figure 1 shows an example of magnetic field measurements at both the PENGUIn  
 120 sites and at the conjugate stations in the Northern hemisphere, taken on 16 November  
 121 2017. The blue lines in this graph show the magnetic fields measured in the Northern  
 122 hemisphere at the sites indicated with the blue labels on the left side, and the red lines  
 123 show the magnetic fields measured in the Southern hemisphere at the sites indicated with  
 124 the red labels on the left side. Site locations are shown in Table 1. All three components  
 125 are graphed. Baseline offsets have been subtracted if present. This figure demonstrates

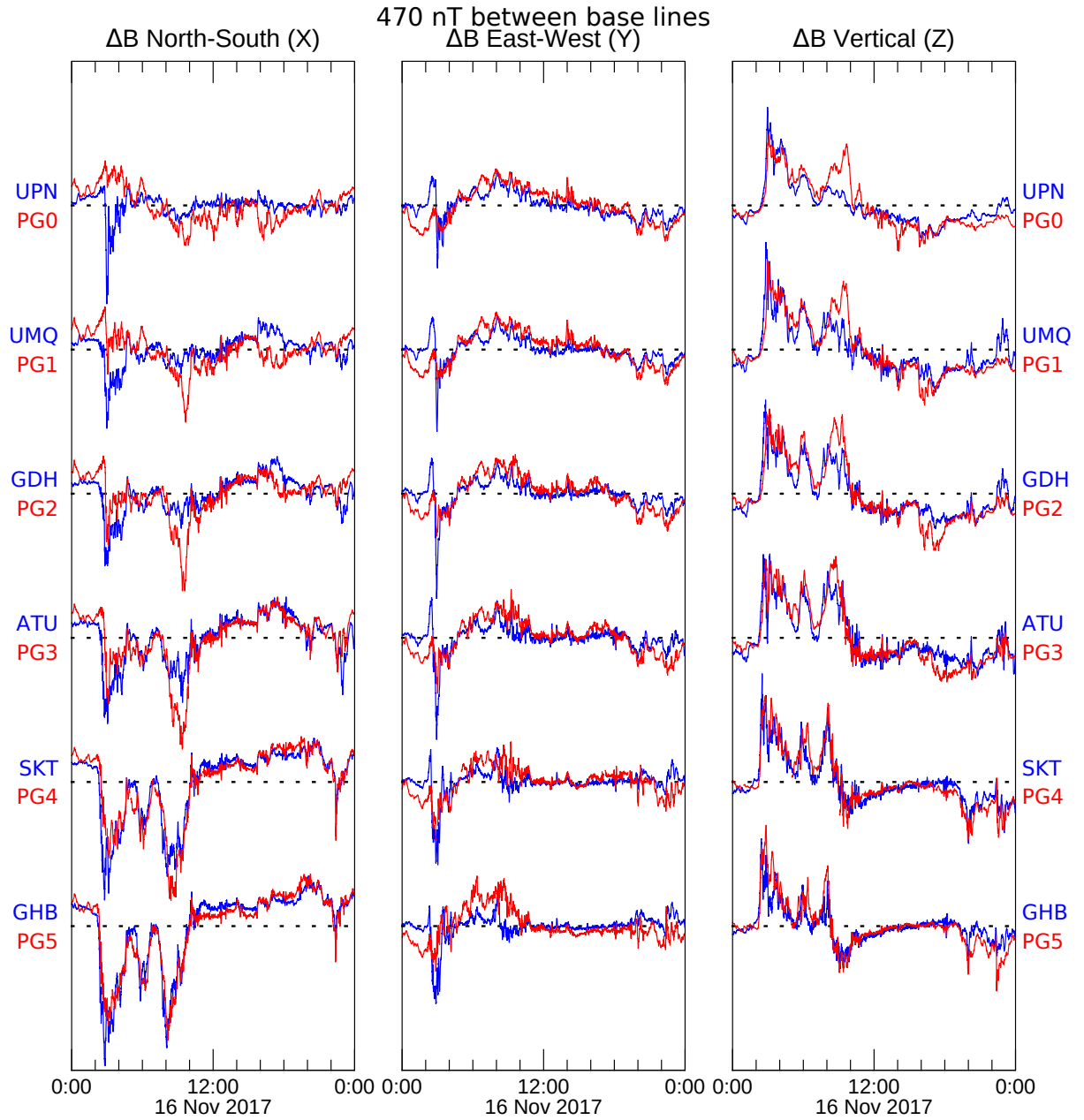


**Figure 1.** Symmetric magnetic fields observed at conjugate locations on 16 November 2017. The blue lines show the magnetic fields measured in the Northern hemisphere at the sites indicated with the blue labels on the left side, and the red lines show the magnetic fields measured in the Southern hemisphere at the sites indicated with the red labels on the left side. Site locations are shown in Table 1.

126 a case where the conjugate measurements are nearly the same, which indicates that the  
 127 conjugate sites can indeed detect similar electrodynamic patterns in opposite hemispheres.

128 For example, the red and blue curves in Figure 1 exhibit very similar behavior at most  
 129 station pairs. The magnetometers are detecting the effects of the Interplanetary Mag-  
 130 netic Field (IMF) merging with the Earth’s magnetic field and the resulting flow of plasma  
 131 and electromagnetic energy in the magnetosphere and ionosphere. Some differences be-  
 132 tween the hemispheres are to be expected due to seasonal differences in conductivity. The  
 133 two most poleward sites at the top of Figure 1 have some disagreements; these sites are  
 134 likely within an area of open magnetic field lines, while the more equatorward sites are  
 135 on closed field lines. The Supplemental Information contains four additional graphs in  
 136 which the conjugate sites have very similar variations.

137 One detail that hadn’t been mentioned until now is the fact that the measurements  
 138 in the southern hemisphere had their eastward and vertical components multiplied by  
 139 -1 in order to obtain the agreements shown. The reasons for these sign changes are il-  
 140 lustrated in Figure 2.

141 Starting with the northward component of  $\Delta B$  in Figure 2(a), a Westward elec-  
 142 trojet, or Hall current, is shown located near midnight in the polar graphs. In the North-  
 143 ern hemisphere the magnetic field underneath this electrojet is pointed away from the  
 144 North pole, so this component has a negative sign. In the Southern hemisphere the mag-  
 145 netic field at ground level is actually located “above” the electrojet when viewed from  
 146 above the North pole, as is the convention with polar graphs of the electrodynamic pat-  
 147 terns that have 0 magnetic local time (MLT) at the bottom, 6 MLT at the right, and  
 148 12 MLT at the top.  $\Delta B_n$  in this case points toward the Southern pole, but since the con-  
 149 vention is that a positive  $\Delta B_n$  points northward, then this component also has a neg-  
 150 ative sign.

151 The eastward component of  $\Delta B$  is illustrated in Figure 2(b). This component typ-  
 152 ically has the smallest magnitude. While the electrojet near midnight MLT is typically  
 153 in the Westward direction, it may have some tilt toward the pole or equator. In 2(b) the  
 154 Hall current flows toward the equator, which produces a positive  $\Delta B_e$  in the Northern  
 155 hemisphere and a negative (westward)  $\Delta B_e$  in the Southern hemisphere. Thus,  $\Delta B_e$  in  
 156 the south needs to have a sign flip in order to match the pattern in the north.

157 Finally, the vertical component of  $\Delta B$  is illustrated in Figure 2(c). Previously D. R. Weimer  
 158 et al. (2010) had found that the vertical component typically has a very good correla-  
 159 tion with the overhead field aligned current (FAC) patterns (D. Weimer, 2001; D. R. Weimer,

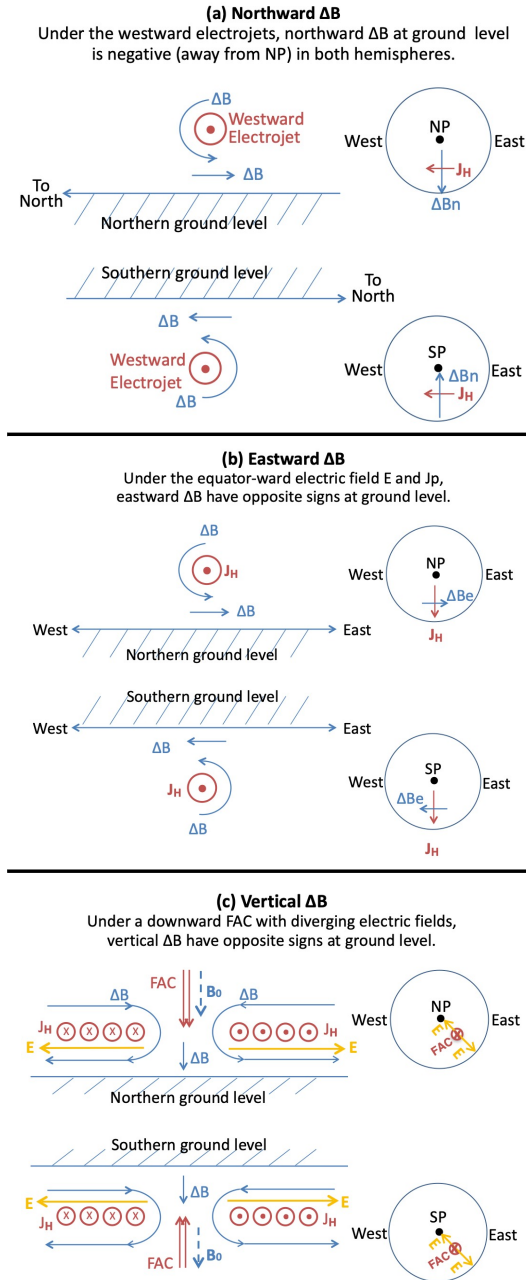


**Figure 2.** Explanation for eastward and vertical sign reversals. (a) Northward  $\Delta B$  underneath a westward electrojet is negative in both hemispheres. (b) Eastward  $\Delta B$  positioned underneath equatorward directed electrojet have opposite signs at the conjugate points. (c) Vertical  $\Delta B$  underneath downward field aligned currents (FAC) also have opposite signs.

160 2005a). In the Northern hemisphere, where the FAC flows into the ionosphere (positive)  
 161 the vertical  $\Delta B_z$  is also positive (downward) and vice versa. Figure 2(c) shows a down-  
 162 ward FAC on the dawn side in both the northern and southern hemispheres on the dawn

163 side, which would be part of the Region 2 system (Iijima & Potemra, 1976). This down-  
 164 ward FAC needs to close through diverging Pedersen currents that are shown in 2(c) as  
 165 producing Pedersen currents and electric fields that point toward the equator on one side  
 166 and toward the pole on the other side. The left side of 2(c) illustrates the Hall currents  
 167 associated with these diverging electric fields, and the magnetic perturbations produced  
 168 by these Hall currents. At the point directly under the FAC this perturbation points to-  
 169 ward the ground in the north (positive  $\Delta B_Z$ ) and away from the ground (negative  $\Delta B_Z$ ).  
 170 Thus,  $\Delta B_Z$  in the south needs to have a sign change in order to match the pattern in  
 171 the north. While the reasons for these sign changes are not intuitively obvious, the data  
 172 shown in Figure 1 and the Supplemental Information confirm that they are necessary.

#### 173 **4 Broken Symmetry**

174 In order for the symmetric magnetic field signatures to be present it is necessary  
 175 for the magnitude of Z component of the IMF to be larger than the Y component. It is  
 176 more common for the Y component to be dominant due to the sector structure of the  
 177 solar wind and IMF. It is known that a strong Y component in the IMF produces a twisted  
 178 magnetotail (White et al., 1998) and magnetopause (Siscoe et al., 2001), and electric po-  
 179 tential patterns that differ between the two hemispheres (Siscoe et al., 2001; D. R. Weimer,  
 180 2005a). Thus, if a non-zero Y component is present with sufficient magnitude then the  
 181 symmetry is broken between the magnetic fields observed at conjugate locations. Ad-  
 182 ditionally, differences in the conductivity, due to unequal solar illumination in summer  
 183 and winter, will also break the symmetry as well as the tilting of the dipole axis toward  
 184 and away from the Sun.

185 Figure 3 shows an example of conjugate measurements from 3 December 2016 that  
 186 do not agree, due to the influence of both the Y component of the IMF and the seasonal  
 187 conductivity and tilt angle differences. The IMF measurements on the same day are shown  
 188 in Figure 4. These data are from the Magnetic Field Instrument (MFI) (Smith et al.,  
 189 1998) on the Advanced Composition Explorer (ACE) spacecraft. The IMF values are  
 190 in the Geocentric Solar Magnetic (GSM) coordinate system. It is seen that the Z com-  
 191 ponent (brown line at bottom) hovers around zero, while varying between -2 and +1 nT.  
 192 The Y component (2nd from bottom, colored turquoise) varies between 1 and 4 nT. The  
 193 solar wind velocity is plotted with the purple line in the third row from the bottom us-  
 194 ing data from the Solar Wind Electron, Proton, and Alpha Monitor (SWEPAM) on ACE

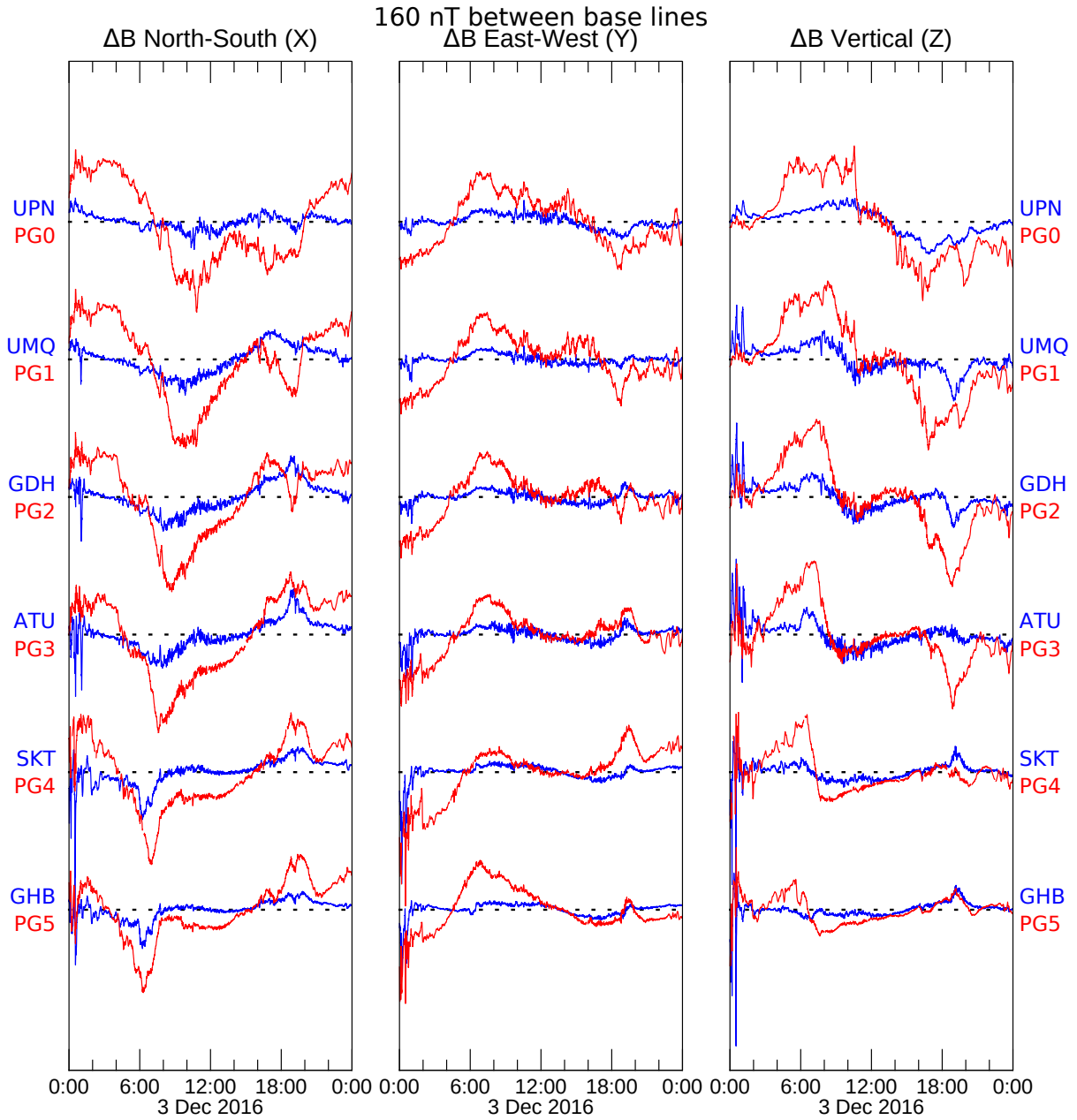


**Figure 3.** Unequal magnetic fields observed at conjugate locations on 3 December 2016. The blue lines show the magnetic fields measured in the Northern hemisphere at the sites indicated with the blue labels on the left side, and the red lines show the magnetic fields measured in the Southern hemisphere at the sites indicated with the red labels on the left side. Site locations are shown in Table 1.

195 (McComas et al., 1998). In Geocentric Solar Ecliptic (GSE) coordinates, the solar wind  
 196 is moving in the -X direction (toward the Earth) at a fairly steady velocity of 300 km/sec.

197 The timeline on the abscissa axis indicates when the measurements were taken at the  
 198 location of the ACE satellite, which is about  $240R_E$  sunward from the Earth. The de-  
 199 lay in time required for the solar wind, and the magnetic field that is embedded within,  
 200 to reach the bow shock of the Earth is approximately 80 min, as shown with the green  
 201 line at the top part of Figure 3.

202 The differences between the magnetic fields seen in the opposite hemispheres can  
 203 be attributed to both the dominant Y component of the IMF as well as conductivity, with  
 204 the southern hemisphere getting much more solar illumination in early December. To  
 205 better understand the behavior of the measured magnetic fields we turn our focus to the  
 206 time period of 7:00 to 19:00 UT on 3 December 2016. Figure 5 shows the Northward com-  
 207 ponent of  $\Delta B_X$  (northward) during this time at the four most poleward PENGUIn sites  
 208 (PG0–PG3) that are shown with the red lines in the bottom four panels in Figure 3. The  
 209 measurements at their conjugate counterparts in the Northern hemisphere are drawn in  
 210 blue. The top two rows shows the Y and Z components of the IMF that have been time  
 211 shifted by 78.1 min, the mean value of the time delay (top of Figure 4) during this in-  
 212 terval. For future reference, marks at 8:00, 12:00, and 18:00 UT are indicated with the  
 213 superposed thin lines.

214 Figure 6 shows maps of ground-level magnetic perturbation patterns and ionospheric  
 215 electric potentials at the three times on 3 December 2016 which help to explain the ob-  
 216 served variations. The maps in the top and third row show the northward component  
 217 of  $\Delta B$  in the Northern and Southern hemispheres respectively that are derived using the  
 218 empirical model by D. R. Weimer (2013). The maps in the second and forth (bottom)  
 219 rows show the electric potential patterns from the empirical model by D. R. Weimer (2005b).  
 220 The maps are generated using the mean of the IMF and solar wind values over the pre-  
 221 vious 20 minutes, after adding another 20 minutes to the propagation delay, that accounts  
 222 for transmission of the electrodynamic signal through the bow shock and then from the  
 223 magnetopause to the polar ionospheres (D. R. Weimer et al., 2010). The Southern hemi-  
 224 sphere maps use IMF  $B_Y$  values in the model inputs that have their signs flipped from  
 225 the values used in north, and the dipole tilt angle is also reversed.

226 These maps are intended to show the context of the magnetic field measurements  
 227 with respect to the mapped patterns, rather than for any comparison of exact values.  
 228 It is seen in Figure 6(a) that at 08:00 UT the northern chain is situated in a region of

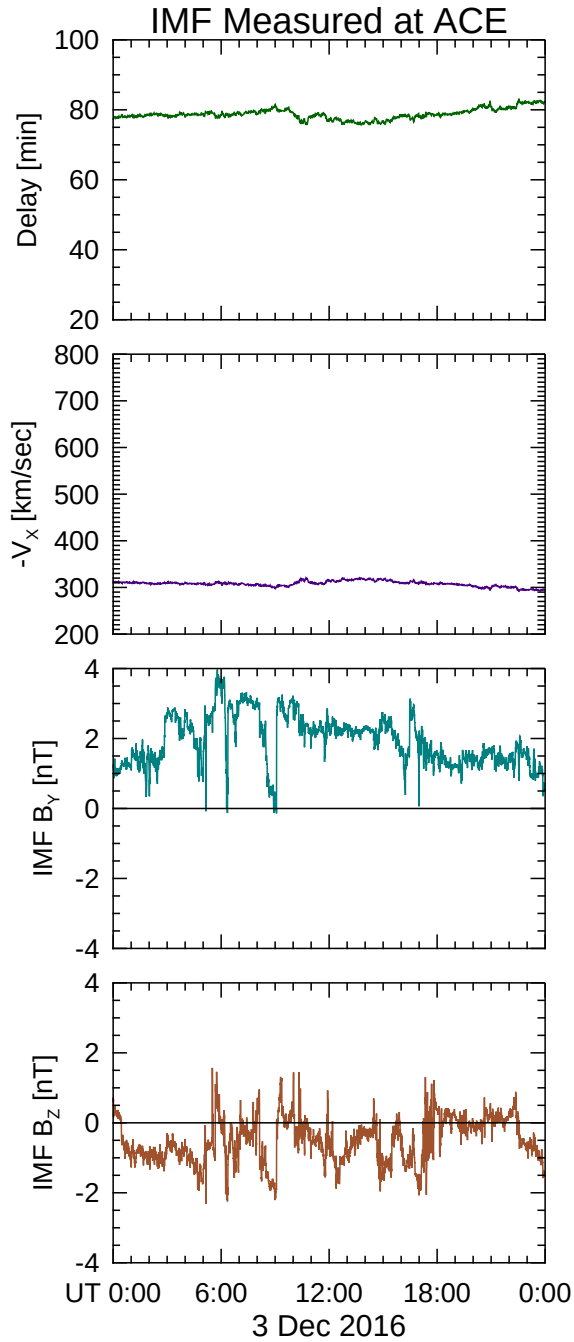


**Figure 4.** IMF measurements taken on the ACE satellite, 3 December 2016. From bottom to top: The Z component of the IMF, drawn in brown (sienna). The Y component of the IMF, colored turquoise. The -X component of the solar wind velocity (purple). At the top, the green line shows the propagation delay, in minutes, from the point of measurement to the Earth.

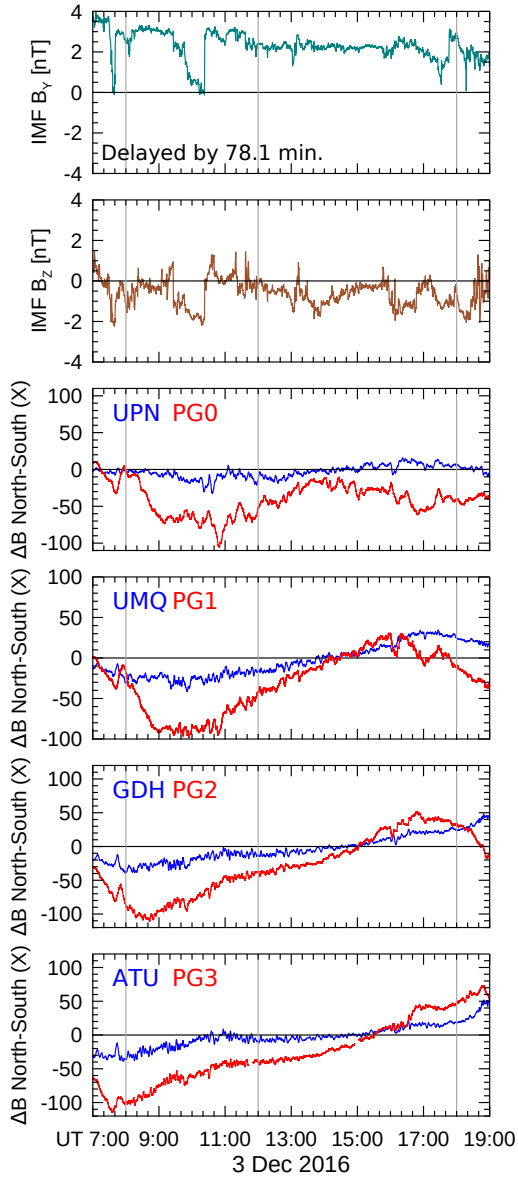


**Figure 5.** Y and Z components of the IMF and the X (Northward) component of  $\Delta B$  at four conjugate locations, from 7:00 to 19:00 UT on 3 December 2016. The upper two rows show the Y and Z components of the IMF, colored turquoise and brown respectively, and shifted in time by 78.1 min. The other four graphs show the Northward component of  $\Delta B$  at the four most poleward PENGUIn sites (drawn in red) and their Northern counterparts (blue). The thin vertical lines mark three times that are referenced in Figure 6.

229 negative  $\Delta B_N$ . At 18:00 UT in 6(c) they have moved to a region of mostly positive  $\Delta B_N$ ,  
 230 with the northernmost end of the chain near the transition between positive and neg-  
 231 ative, in qualitative agreement with the measurements shown in Figure 5. The south-

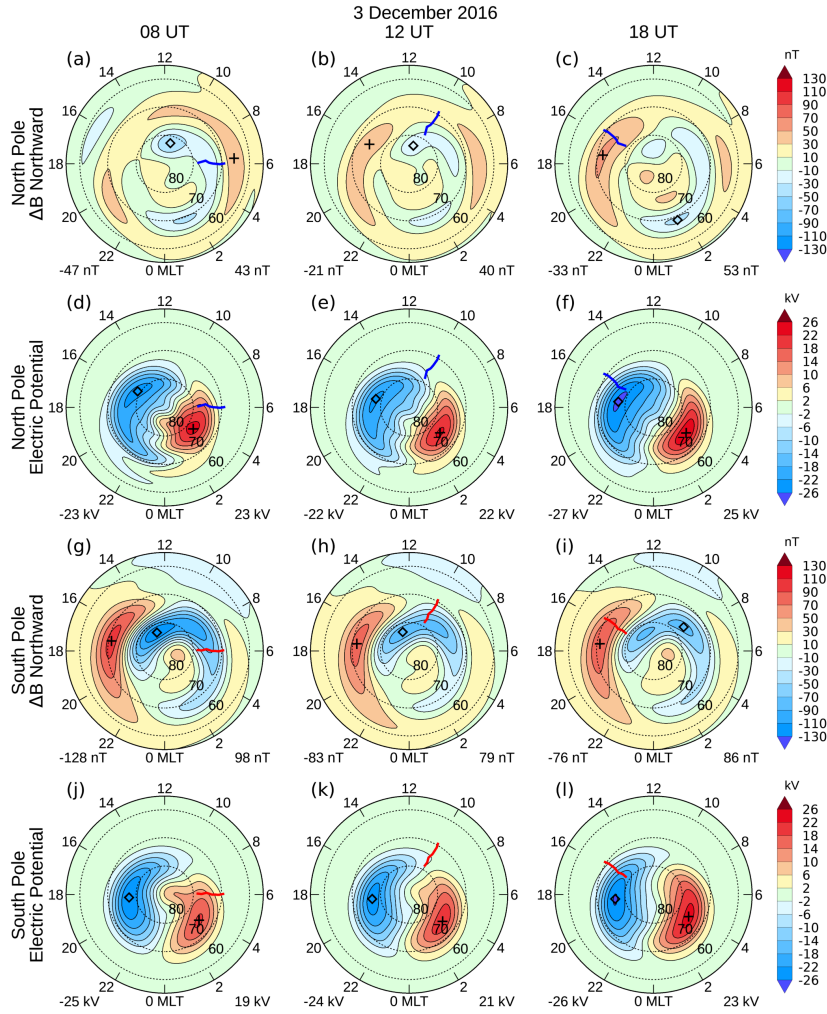


**Figure 6.** Maps of the (Northward) component of  $\Delta B$  and electric potentials in both hemispheres. These maps are for 08:00 UT (left column), 12:00 UT (center column), and 18:00 UT (right column) on 3 December 2016. The maps in the top row show the Northward component of  $\Delta B$  at the three times listed, with the location of the Greenland chain in magnetic latitude-local time coordinates superposed on the map with a blue line. The second row shows the electric potentials in the Northern hemisphere, with the magnetometer locations superposed. The third row shows the Northward component of  $\Delta B$ , with the location of the Antarctic chain marked with a red line. The bottom row shows the electric potentials in the Southern hemisphere. Minimum and maximum values of the mapped quantities are indicated in the lower left and right corners of each polar map.

232 ern chain at 08:00 UT in 6(g) mostly lies in a more strongly negative  $\Delta B_N$ , with the most  
 233 poleward end positioned near a transition to a positive region. At 18:00 UT in 6(i) the

234 southern sites have moved to a region of positive  $\Delta B_N$  at the low latitude end while the  
235 poleward sites cross zero into negative territory, in agreement with Figure 5. Through-  
236 out this day the higher conductivity in the southern hemisphere obviously influences the  
237 larger magnetic field values that are seen. The influence of IMF  $B_Y$  is most apparent  
238 at 18 UT, and the changes seen throughout the day are mostly the result of the sites sim-  
239 ply moving in local time.

## 240 5 IMF $B_Y$ Step Transitions

241 Another case in which the Y component of the IMF has an even greater influence  
242 on the observed asymmetry is shown in Figure 7, in the same format as Figures 1 and  
243 3, from 4 February 2016. The IMF measurements on the same day, 4 February 2016, are  
244 shown in Figure 8, in the same format as Figure 4. The Z component fluctuates around  
245 a value of +5 nT during most of the day, except for a period from approximately 09:00  
246 to 15:00 UT when it drops to less than zero on two occasions. The Y component is in  
247 the range of +5 to +8 nT through most of the day, except for a prominent transition  
248 to -5 nT for just over two hours before flipping back to +5 nT. The solar wind veloc-  
249 ity, shown with the purple line in the third row from the bottom, runs between 400 to  
250 480 km/sec. This velocity results in a time delay for the solar wind to reach the bow shock  
251 of the Earth in approximately 50 min, as shown with the green line in the top row, if it  
252 is assumed that the IMF fluctuations lie within a flat plane that is perpendicular to the  
253 flow direction.

254 As found by D. R. Weimer et al. (2002), the IMF transitions often lie within planes  
255 that are tilted at varying angles with respect to the Earth-Sun line (GSE X axis) rather  
256 than perpendicular, which results in complicated variations in the propagation times.  
257 The magenta-colored line that is superposed in the top row shows the expected time de-  
258 lays that take these tilted orientations into consideration, using the method outlined by  
259 D. R. Weimer and King (2008). Refer to the articles and illustrations therein by J. Borovsky  
260 (2008) and J. E. Borovsky (2018) for a description of the geometrical structure of the  
261 of the IMF that causes the variations in the propagation times. This modification to the  
262 delays is included in Figure 8 due to the need for more accurate timings later in this pa-  
263 per.

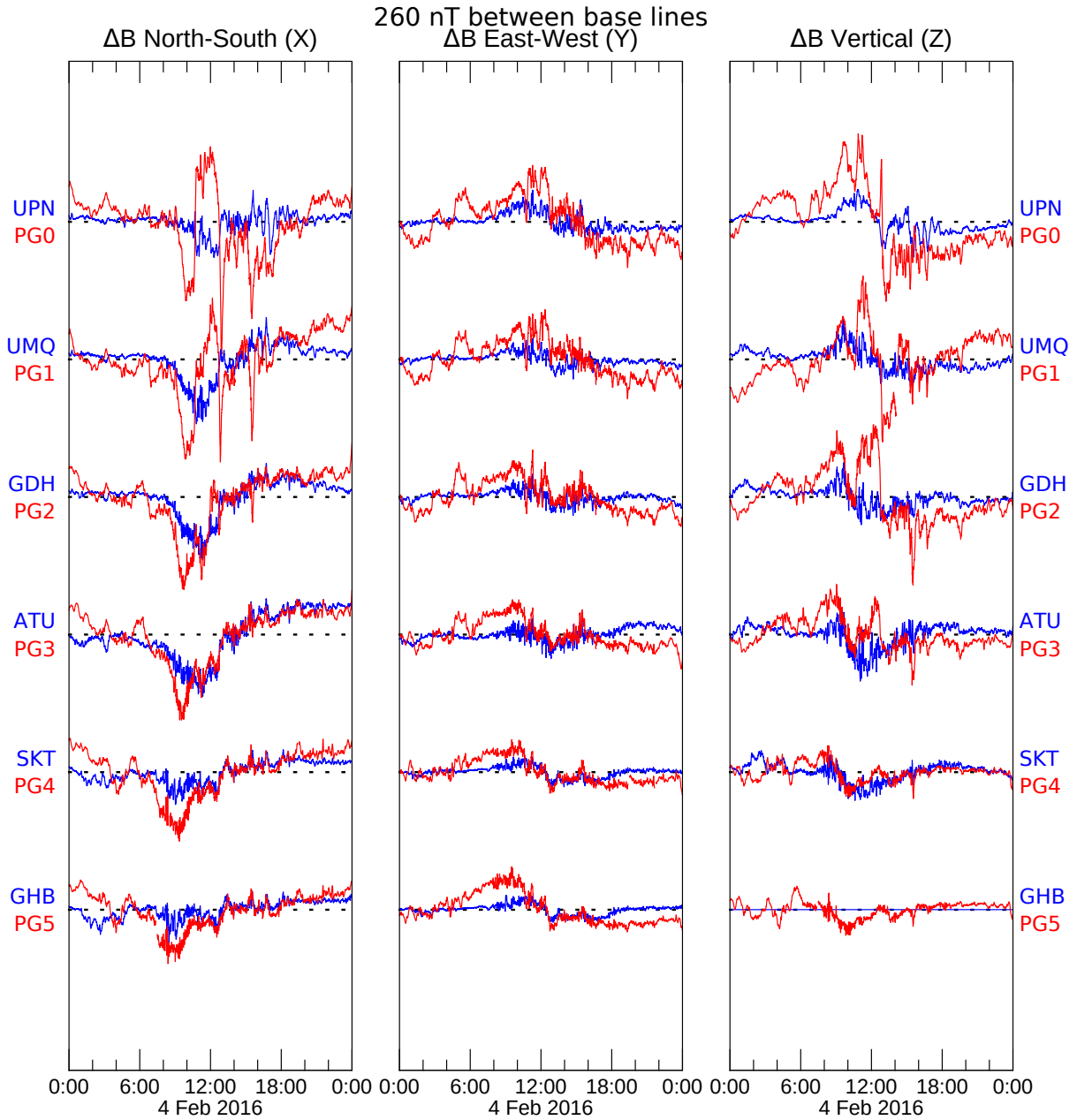


**Figure 7.** Unequal magnetic fields observed at conjugate locations on 4 February 2016. The blue lines show the magnetic fields measured in the Northern hemisphere at the sites indicated with the blue labels on the left side, and the red lines show the magnetic fields measured in the Southern hemisphere at the sites indicated with the red labels on the left side. Site locations are shown in Table 1.

264

Figure 9 shows a closer look at the time period around the IMF  $B_Y$  transitions on

265

4 February 2016, from 09:00 UT to 14:00 UT. The format of this figure is similar to that

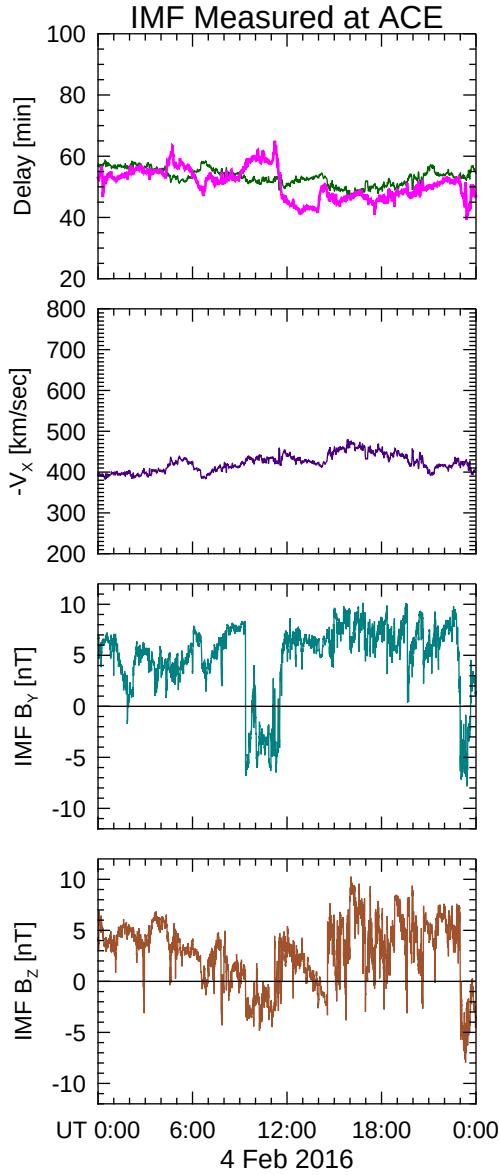


**Figure 8.** IMF measurements taken on the ACE satellite, 4 February 2016. From bottom to top: The Z component of the IMF, drawn in brown. The Y component of the IMF, colored turquoise. The X component of the solar wind velocity (purple). At the top, the green line shows the “flat plane” propagation delay, in minutes from the point of measurement at L1 to the Earth, and the superposed magenta line show the propagation delay that accounts for phase front tilt angles.

266

in Figure 5, with the four bottom rows showing the northward component of  $\Delta B$  at the

267

four most poleward PENGUIn sites (PG0–PG3) drawn with the red lines while the North-

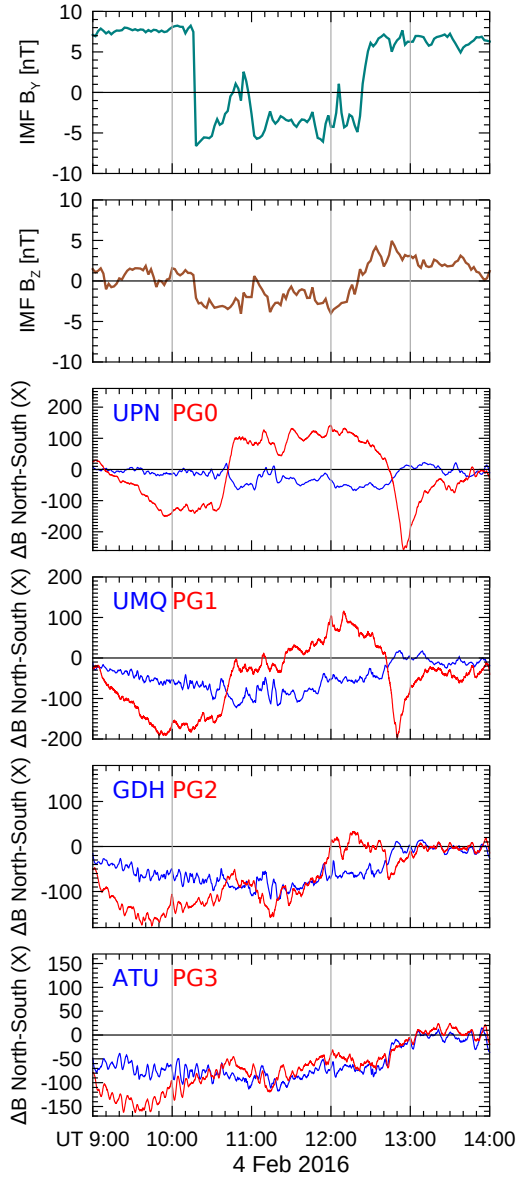


**Figure 9.** Y component of the IMF and the X (Northward) component of  $\Delta B$  at four conjugate locations, from 09:00 to 14:00 UT on 4 February 2016. The upper two rows show the Y and Z component of the IMF drawn in turquoise and brown, shifted in time to the bow shock using variable lags. The other four graphs show the Northward component of  $\Delta B$  at the four most poleward PENGUIn sites (drawn in red) and their Northern counterparts (blue). Dotted lines on the time axis mark three times at 10:00, 12:00, and 13:00 UT that are referenced in Figure 10.

268 ern hemisphere data are drawn in blue. The top two rows shows the Y and Z compo-  
 269 nents of the IMF drawn with turquoise and brown colors. These IMF data have been  
 270 shifted in time to the position of the solar wind bow shock in front of the Earth, using

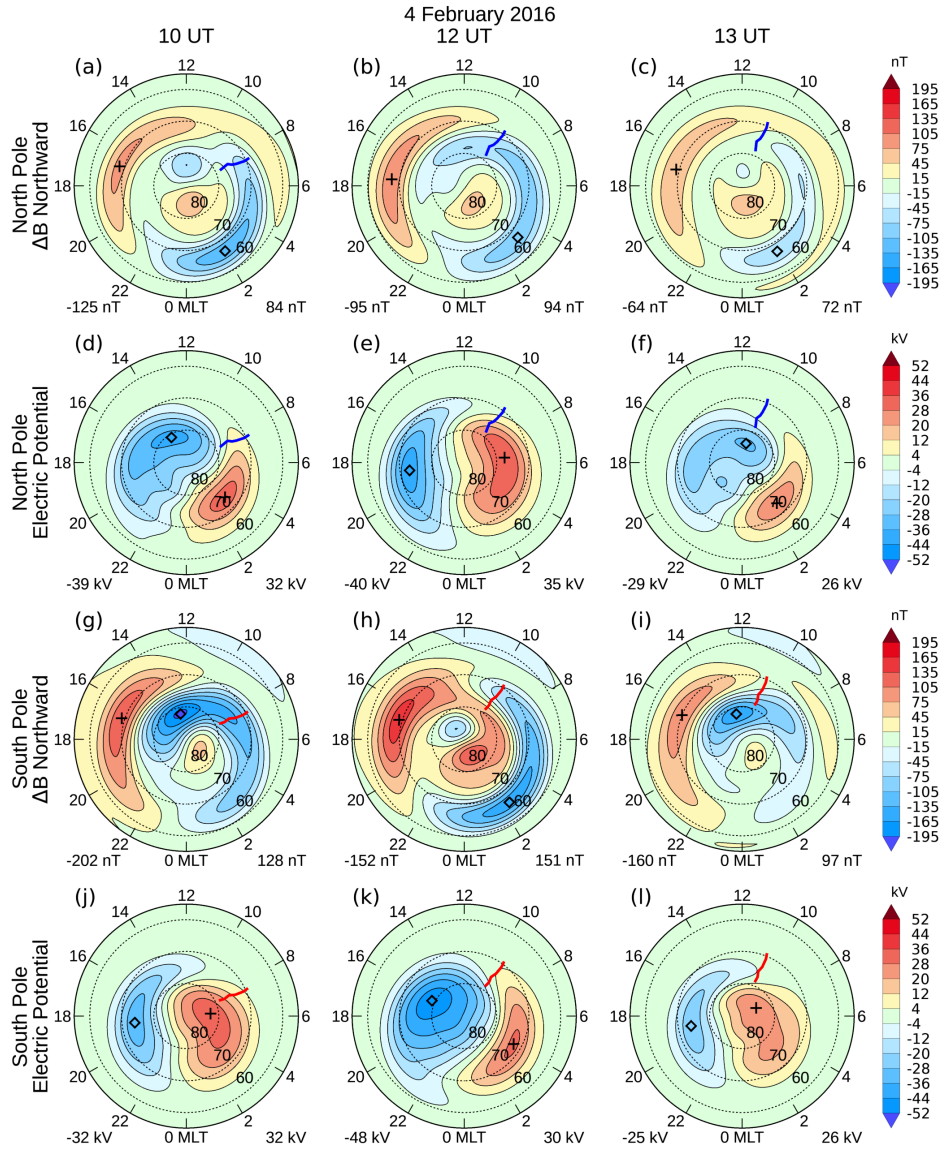


**Figure 10.** Maps of the (Northward) component of  $\Delta B$  and electric potentials in both hemispheres. These maps are for 10:00 UT (left column), 12:00 UT (center column), and 13:00 UT (right column) on 4 February 2016. The format of this figure is the same as Figure 6.

271 the variable timings shown in Figure 8. Reference marks at 10:00, 12:00, and 13:00 UT  
 272 are indicated on the horizontal axis using dotted lines. The first mark at 10:00 UT is just  
 273 before IMF Y flips from positive to negative, 12:00 UT is near the end of the negative  
 274 time interval (during which the electrodynamic pattern has had time to reconfigure), and  
 275 13:00 UT is approximately a half-hour after the transition of IMF Y back to a positive  
 276 value.

277 Figure 10 shows maps of ground-level magnetic perturbation patterns and iono-  
 278 spheric electric potentials on 4 February 2016 at the three times just mentioned. The  
 279 format of this figure is the same as in Figure 6. As before, the maps in this figure show  
 280 an overview of the northern and southern magnetometer chain locations with respect to  
 281 the global electric potential and magnetic perturbation patterns. At 10:00 UT the north-  
 282 ern chain is situated in a region of negative  $\Delta B_N$ , except at the most poleward site which  
 283 is near zero, as seen in 10(a). The measurements shown with the blue lines in Figure 9  
 284 at this time are in agreement, with the UPN site being located the most poleward. The  
 285 southern chain in 10(g) is positioned entirely within a region of negative  $\Delta B_N$  but hav-  
 286 ing a larger magnitude. This southern chain is positioned within the dawn electric po-  
 287 tential cell in 10(j), while the northern chain in 10(d) is at the dayside end of the dawn  
 288 cell and extending into the anti-sunward plasma flow.

289 In 10(b) at 12:00 UT, after IMF  $B_Y$  flips from positive to negative, the northern  
 290 chain is now in a region of more strongly negative  $\Delta B_N$ . Figure 10(h) shows that the  
 291 southern chain at this time is in the negative region at the more equatorward end, while  
 292 the more poleward end is in the positive part of the map, in agreement with data shown  
 293 in Figure 9.

294 After the IMF  $B_Y$  flips back to positive, by 13:00 UT the northern chain extends  
 295 from weakly positive at the low latitude end to near zero at the poleward end, as illus-  
 296 trated with the blue lines in Figures 9 and 10(c). At the same time, 10(i) shows that the  
 297 southern chain transitions from near zero at the equatorward end to strongly negative  
 298 at the poleward end, also in agreement with Figure 9.

## 299 6 Time Lags and Response Times

300 The sharp transitions in IMF  $B_Y$  on 4 February 2016 provide an opportunity to  
 301 reexamine the time lags between changes in the IMF and the observed ground-level mag-  
 302 netic response. From enlarged versions of Figure 9 (not shown) it was found that  $B_Y$   
 303 flips from positive to negative at 10:17 UT while the magnetic field at the PG0 and PG1  
 304 sites start to increase from negative toward positive 18 min later, at 10:35 UT. These  
 305 transitions reach their peak 13 min later at 10:48 UT. The lags at the northern sites UPN  
 306 and UMQ are similar, but difficult to ascertain with certainty due to the much smaller

307 variations in the winter hemisphere. At the more equatorward sites in both hemispheres  
 308 the changes in the magnetic fields are unremarkable.

309 At the next IMF transition  $B_Y$  crosses zero going positive at 12:23 UT, while at  
 310 the same time  $B_Z$  is also moving from negative to positive. At southern sites PG0 and  
 311 PG1 the measured  $\Delta B_N$  have been decreasing since 12:00 UT, and then at 12:41 UT the  
 312 rate of change accelerates. Again, this change occurs 18 min after the IMF  $B_Y$  flip. The  
 313 most negative value is reached 14 min later at 12:55 UT at PG0, and after 9 min at 12:50  
 314 UT at PG1, with similar but much smaller responses seen at the northern conjunction  
 315 sites. Speculating, PG1 may have reacted faster than PG0 by being located closer to the  
 316 center of the anti-sunward convection “throat” in Figure 10(k).

## 317 **7 Discussion and Conclusion**

318 It has long been assumed that the ionospheres in the northern and southern hemi-  
 319 spheres have similar electrodynamic patterns. Under some conditions the magnetic per-  
 320 turbations at opposite ends of the magnetic field lines are expected to be similar. The  
 321 placement of the PENGUIn magnetometers at locations conjugate to stations on the west  
 322 coast of Greenland provided an opportunity to verify these assumptions. The results pre-  
 323 sented here (and in Supplemental Information figures) confirm that the conjugate sites  
 324 do have identical or similar (symmetric) magnetic perturbations under the right condi-  
 325 tions. We’ve shown that sign reversals are required for the Y (eastward) and Z (down-  
 326 ward) components in order to obtain this agreement. More often than not, a dominant  
 327 IMF  $B_Y$  can break the symmetry, as well as the presence of unequal conductivities in  
 328 the opposite hemispheres. Statistical maps of electric potentials and magnetic pertur-  
 329 bations are shown to be useful for explaining the temporal changes that occur in both  
 330 hemispheres. During the course of the day, it is often the movement of magnetometers  
 331 in local time that causes the observed variations. It would be possible to use numerical  
 332 simulations and other models in a similar manner to provide the context of the magne-  
 333 tometer locations with respect to the global patterns.

334 In one event the Y component of the IMF flipped from strongly positive to strongly  
 335 negative, and back again about two hours later, while the northern and southern mag-  
 336 netometer chains were approaching noon in local time. This fortuitous occurrence pro-  
 337 vided a unique opportunity to observe the broken symmetry at the conjugate locations

338 and to measure the time lags between the IMF transitions and the resulting magnetic  
339 field reaction. It was found that the magnetic fields at most poleward sites started to  
340 respond to the sudden IMF changes after 18 min, a measure of the time it takes for the  
341 electromagnetic signal in the solar wind and embedded IMF to reach the magnetopause,  
342 after travel from the bow shock through the magnetosheath, and then propagate along  
343 magnetic field lines to the polar ionospheres. The propagation delay is also referred to  
344 as the “communication time,” which can be in the range of 8–14 min (Ridley et al., 1998).  
345 An additional 9 to 14 min is required for the magnetic perturbations to complete the tran-  
346 sition. The time delays are longer at the more equatorward locations. These results agree  
347 with previous findings by Ridley et al. (1998), D. R. Weimer et al. (2010), and references  
348 therein, but with better temporal resolution.

349 Space science investigations have long relied on magnetometer measurements in the  
350 northern hemisphere to indirectly observe the flow of currents in the ionosphere and mag-  
351 netosphere. It has only been more recently that it has been possible to acquire magnetic  
352 field measurements in the southern polar region in order to observe hemispheric simi-  
353 larities and differences. While there are substantial engineering and logistical challenges  
354 in putting magnetometers on the Antarctic plateau (Clauer et al., 2014), the expansion  
355 and maintenance of such infrastructure will advance future research which will yield in-  
356 sight into the causes and consequences of multi-scale hemispheric asymmetries”

## 357 **Open Research Section**

358 The magnetometer data are available at these web sites:

359 <http://mist.nianet.org>

360 <http://128.173.89.68:48000/>

361 <https://www.space.dtu.dk/English/Research/>

362 <https://ftp.space.dtu.dk/data/>

363 The interplanetary magnetic field and solar wind measurements from the ACE space-  
364 craft can be obtained at <https://cdaweb.gsfc.nasa.gov/pub/data/ace/>

365 The Weimer 2005 electric potential model is available at [https://doi.org/10.5281/](https://doi.org/10.5281/zenodo.2530324)  
366 [zenodo.2530324](https://doi.org/10.5281/zenodo.2530324), and maps produced by the Weimer 2013 magnetic perturbation model  
367 are available at <https://doi.org/10.5281/zenodo.3985988>.

## 368 **Acknowledgments**

369           This work was funded by NSF grants OPP-1543364, OPP-1744828, and AGS-2027168  
370 to Virginia Tech. MDH was supported by NSF grant AGS-2027210.

## References

- 371
- 372 Borovsky, J. (2008). The flux-tube texture of the solar wind: strands of the mag-  
 373 netic carpet at 1 AU? *J. Geophys. Res.*, *113*. doi: 10.1029/2007JA012684
- 374 Borovsky, J. E. (2018). The spatial structure of the oncoming solar wind at Earth  
 375 and the shortcomings of a solar-wind monitor at L1. *Journal of Atmospheric  
 376 and Solar-Terrestrial Physics*, *177*, 2 – 11. doi: 10.1016/j.jastp.2017.03.014
- 377 Clauer, C. R., Kim, H., Deshpande, K., Xu, Z., Weimer, D., Musko, S., ... Ri-  
 378 dley, A. J. (2014). An autonomous adaptive low-power instrument plat-  
 379 form (AAL-PIP) for remote high-latitude geospace data collection. *Geo-  
 380 scientific Instrumentation, Methods and Data Systems*, *3*(2), 211–227. Re-  
 381 trieved from <https://gi.copernicus.org/articles/3/211/2014/> doi:  
 382 10.5194/gi-3-211-2014
- 383 Hartinger, M. D., Clauer, C. R., & Xu, Z. (2016, October). Space weather from a  
 384 southern point of view. *Eos*, *97*. doi: 10.1029/2016EO061791
- 385 Hartinger, M. D., Xu, Z., Clauer, C. R., Yu, Y., Weimer, D. R., Kim, H., ... Willer,  
 386 A. N. (2017). Associating ground magnetometer observations with cur-  
 387 rent or voltage generators. *Journal of Geophysical Research: Space Physics*,  
 388 *122*(7), 7130–7141. Retrieved from [https://agupubs.onlinelibrary.wiley  
 389 .com/doi/abs/10.1002/2017JA024140](https://agupubs.onlinelibrary.wiley.com/doi/abs/10.1002/2017JA024140) doi: [https://doi.org/10.1002/  
 390 2017JA024140](https://doi.org/10.1002/2017JA024140)
- 391 Iijima, T., & Potemra, T. A. (1976). The amplitude distribution of field aligned  
 392 currents at northern high latitudes observed by Triad. *J. Geophys. Res.*, *81*,  
 393 2165–2174. doi: 10.1029/JA081i013p02165
- 394 Laundal, K., Cnossen, I., Milan, S., Haaland, S., Coxon, J., Pedatella, N., ... Reis-  
 395 tad, J. (2017). North–South asymmetries in Earth’s magnetic field. *Space  
 396 Science Reviews*, *206*, 225–257. Retrieved from [https://doi.org/10.1007/  
 397 s11214-016-0273-0](https://doi.org/10.1007/s11214-016-0273-0) doi: 10.1007/s11214-016-0273-0
- 398 Martines-Bedenko, V. A., Pilipenko, V. A., Hartinger, M. D., Engebretson,  
 399 M. J., Lorentzen, D. A., & Willer, A. N. (2018). Correspondence be-  
 400 tween the latitudinal ulf wave power distribution and auroral oval in con-  
 401 jugate ionospheres. *Sun and Geosphere*, *13*(1), 41–47. Retrieved from  
 402 <https://par.nsf.gov/biblio/10057802>
- 403 McComas, D. J., Bame, S. J., Barber, P., Feldman, W. C., Phillips, J. L., & Riley,

- 404 P. (1998). Solar wind electron, proton, and alpha monitor (SWEPAM) on  
 405 the Advanced Composition Explorer. In C. T. Russell, R. A. Mewaldt, &  
 406 T. T. V. Rosengvinge (Eds.), *The Advanced Composition Explorer Mission*.  
 407 Dordrecht: Springer. doi: [https://doi.org/10.1007/978-94-011-4762-0\\_20](https://doi.org/10.1007/978-94-011-4762-0_20)
- 408 Ostgaard, N., & Laundal, K. M. (2012). Auroral asymmetries in the conjugate hemi-  
 409 spheres and interhemispheric currents. In *Auroral phenomenology and magne-*  
 410 *tospheric processes: Earth and other planets* (pp. 99–112). American Geophys-  
 411 ical Union (AGU). Retrieved from [https://agupubs.onlinelibrary.wiley](https://agupubs.onlinelibrary.wiley.com/doi/abs/10.1029/2011GM001190)  
 412 [.com/doi/abs/10.1029/2011GM001190](https://agupubs.onlinelibrary.wiley.com/doi/abs/10.1029/2011GM001190) doi: 10.1029/2011GM001190
- 413 Richmond, A. D. (1995). Ionospheric electrodynamics using magnetic apex coordi-  
 414 nates. *J. Geomag. Geoelectr.*, *47*, 191. doi: 10.5636/jgg.47.191
- 415 Ridley, A. J., Lu, G., Clauer, C. R., & Papitashvili, V. O. (1998). A statisti-  
 416 cal study of the ionospheric convection response to changing interplanetary  
 417 magnetic field conditions using the assimilative mapping of ionospheric electro-  
 418 dynamics technique. *J. Geophys. Res.*, *103*(A3), 4023–4039. Retrieved from  
 419 <https://doi.org/10.1029/97JA03328> doi: 10.1029/97JA03328
- 420 Siscoe, G. L., Erickson, G. M., Sonnerup, B. U. O., Maynard, N. C., Siebert, K. D.,  
 421 Weimer, D. R., & White, W. W. (2001). Global role of  $E_{\parallel}$  in magnetopause  
 422 reconnection: An explicit demonstration. *J. Geophys. Res.*, *106*(A7), 13015–  
 423 13022. Retrieved from <https://doi.org/10.1029/2000JA000062> doi:  
 424 10.1029/2000JA000062
- 425 Smith, C. W., L’Heureux, J., Ness, N. F., Acuna, M. H., Burlaga, L. F., & Scheifele,  
 426 J. (1998). The ACE Magnetic Field Experiment. In C. T. Russell,  
 427 R. A. Mewaldt, & T. T. V. Rosengvinge (Eds.), *The Advanced Composi-*  
 428 *tion Explorer Mission*. Dordrecht: Springer. doi: [https://doi.org/10.1007/](https://doi.org/10.1007/978-94-011-4762-0_21)  
 429 [978-94-011-4762-0\\_21](https://doi.org/10.1007/978-94-011-4762-0_21)
- 430 VanZandt, T. E., Clark, W. L., & Warnock, J. M. (1972). Magnetic apex coordi-  
 431 nates: A magnetic coordinate system for the ionospheric  $f_2$  layer. *Journal Of*  
 432 *Geophysical Research-Space Physics*, *77*, 2406. doi: 10.1029/JA077i013p02406
- 433 Weimer, D. (2001). Maps of field-aligned currents as a function of the interplanetary  
 434 magnetic field derived from Dynamic Explorer 2 data. *J. Geophys. Res.*, *106*,  
 435 12,889. doi: 10.1029/2000JA000295
- 436 Weimer, D. R. (2005a). Improved ionospheric electrodynamic models and applica-

- 437           tion to calculating Joule heating rates. *J. Geophys. Res.*, *110*. doi: 10.1029/  
438           2004JA010884
- 439 Weimer, D. R. (2005b). Predicting surface geomagnetic variations using ionospheric  
440           electrodynamical models. *J. Geophys. Res.*, *110*. doi: 10.1029/2005JA011270
- 441 Weimer, D. R. (2013). An empirical model of ground-level geomagnetic pertur-  
442           bations. *Space Weather*, *11*, 107–120. Retrieved from [https://doi.org/10](https://doi.org/10.1002/swe.20030)  
443           .1002/swe.20030 doi: 10.1002/swe.20030
- 444 Weimer, D. R., Clauer, C. R., Engebretson, M. J., Hansen, T. L., Gleisner, H.,  
445           Mann, I., & Yumoto, K. (2010). Statistical maps of geomagnetic perturbations  
446           as a function of the interplanetary magnetic field. *J. Geophys. Res.*, *115*. doi:  
447           10.1029/2010JA015540
- 448 Weimer, D. R., & King, J. H. (2008). Improved calculations of interplanetary mag-  
449           netic field phase front angles and propagation time delays. *J. Geophys. Res.*,  
450           *113*. doi: 10.1029/2007JA012452
- 451 Weimer, D. R., Ober, D. M., Maynard, N. C., Burke, W. J., Collier, M. R., McCo-  
452           mas, D. J., ... Smith, C. W. (2002). Variable time delays in the propaga-  
453           tion of the interplanetary magnetic field. *J. Geophys. Res.*, *107*((A8)). doi:  
454           10.1029/2001JA009102
- 455 White, W. W., Siscoe, G. L., Erickson, G. M., Kaymaz, Z., Maynard, N. C.,  
456           Siebert, K. D., ... Weimer, D. R. (1998). The magnetospheric sash and  
457           the cross-tail S. *Geophys. Res. Lett.*, *25*, 1605–1608. Retrieved from  
458           <https://doi.org/10.1029/98GL50865> doi: 10.1029/98GL50865
- 459 Xu, Z., Hartinger, M. D., Clauer, C. R., Peek, T., & Behlke, R. (2017). A  
460           comparison of the ground magnetic responses during the 2013 and 2015  
461           St. Patrick’s Day geomagnetic storms. *Journal of Geophysical Research:*  
462           *Space Physics*, *122*(4), 4023–4036. Retrieved from <https://agupubs>  
463           .[onlinelibrary.wiley.com/doi/abs/10.1002/2016JA023338](https://agupubs.onlinelibrary.wiley.com/doi/abs/10.1002/2016JA023338) doi:  
464           <https://doi.org/10.1002/2016JA023338>
- 465 Xu, Z., Hartinger, M. D., Oliveira, D. M., Coyle, S., Clauer, C. R., Weimer, D.,  
466           & Edwards, T. R. (2020). Interhemispheric asymmetries in the ground  
467           magnetic response to interplanetary shocks: The role of shock impact an-  
468           gle. *Space Weather*, *18*(3), e2019SW002427. Retrieved from <https://>  
469           [agupubs.onlinelibrary.wiley.com/doi/abs/10.1029/2019SW002427](https://agupubs.onlinelibrary.wiley.com/doi/abs/10.1029/2019SW002427) doi:

<https://doi.org/10.1029/2019SW002427>